

File ID 226009  
Filename 2: Experimental techniques

---

SOURCE (OR PART OF THE FOLLOWING SOURCE):

Type Dissertation  
Title Spatial correlations and deformation modes in sheared colloidal glasses  
Author V.K. Chikkadi  
Faculty Faculty of Science  
Year 2011  
Pages vi, 128  
ISBN 9789491211768

FULL BIBLIOGRAPHIC DETAILS:

<http://dare.uva.nl/record/387717>

---

*Copyright*

*It is not permitted to download or to forward/distribute the text or part of it without the consent of the author(s) and/or copyright holder(s), other than for strictly personal, individual use.*

---

---

# 2 Experimental techniques

---

## 2.1 Colloids

Colloids are nanometer to micron sized particles that are dispersed in a continuous phase. Colloidal systems are ubiquitous in nature in various forms. A few familiar examples are fogs, mists, smokes where fine liquid droplets are dispersed in a gas - *aerosols*, dispersions of fat in an aqueous phase - *milk*, emulsions, paint, mud, slurries, where solid particles dispersed in a liquid medium - *sols*. An illustration of the length scales of various materials that fall in the colloidal domain is shown in Fig.2.1 [62]. We investigate colloidal particles suspended in a liquid; because of their small size, these particles exhibit Brownian motion. The simplest form of such a colloidal suspension consists of hard spherical particles that exhibit no interaction until they touch. This hard-sphere interaction, in the presence of thermal fluctuations, is sufficient to produce a variety of phases such as fluid, crystalline and glassy states of matter. These phases are analogous to the states of matter observed in atomic and molecular physics, but occur over much larger length scales, and longer time scales [14]. The relatively large length scales, and long time scales make it easy for these phases to be studied in real-space and real time. Therefore quantities that are experimentally difficult to observe in atomic systems can be measured with relative ease in colloidal systems through the use of direct imaging techniques, such as confocal microscopy [63, 64], or indirect imaging techniques, such as light scattering [65, 66] as well as rheology [67].

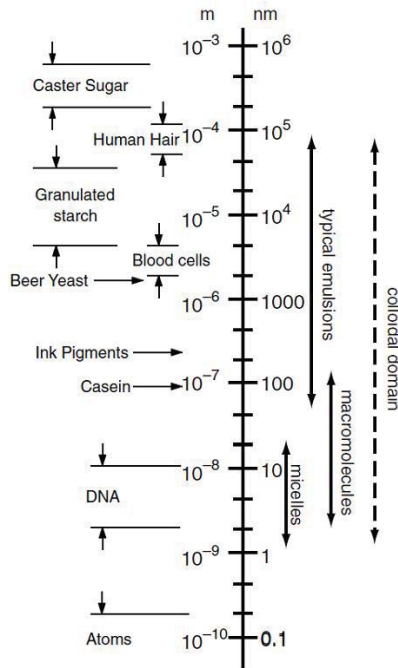


Figure 2.1: The colloidal domain : the dimensions and typical examples of materials that fall in the colloidal size range [62].

## 2.2 Hard Sphere Colloids

The simplest model colloidal system is that of mono-disperse, Brownian hard spheres. These hard spheres are non-interacting as long as they do not touch, and infinitely repulsive on contact. The parameter that determines the phase behavior of hard sphere systems is the volume fraction of the spheres,  $\phi$ , given by

$$\phi = \frac{N \times V_p}{V_{tot}}$$

where  $N$  is the number of particles,  $V_p = (4/3)\pi a^3$  is the volume of a single particle of radius  $a$  and  $V_{tot}$  is the total volume of the continuous phase and all the particles.

The time scale in colloidal systems can be defined from the perspective of the particles. In the dilute limit when the particles exhibit free

Brownian motion, the mean square displacement  $\langle r^2 \rangle$  of the particles increases linearly with time

$$\langle r^2 \rangle = 6D\tau, \quad (2.1)$$

where  $D$  is the diffusion coefficient. The diffusion coefficient for a spherical particle in a dilute solution is given by the ratio of the thermal energy  $k_B T$  and the frictional drag  $f$ , on the particles.

$$D = \frac{k_B T}{f}, \text{ where} \quad (2.2)$$

$$f = 6\pi\eta_0 a. \quad (2.3)$$

Here,  $k_B$  is the Boltzmann constant,  $T$  is the absolute temperature,  $\eta_0$  is the solvent viscosity and  $a$  is the particle radius. The time required by the particle to move its own size defines the characteristic time scale for the colloidal suspension, which is often referred as Brownian time scale  $\tau_B$

$$\tau_B = \frac{\pi\eta_0 a^3}{k_B T}. \quad (2.4)$$

The above relation is valid for very dilute systems under quiescent conditions. It does not include any body forces acting on the particle such as gravity or mechanical or thermal convection. It also neglects the hydrodynamic interactions between the particles that may influence the diffusion and the effective viscosity by several orders of magnitude. Interactions in more concentrated suspensions can be taken into account by substituting the effective viscosity of the material  $\eta$  for the solvent viscosity [67].

$$\tau = \frac{\pi\eta a^3}{k_B T} \quad (2.5)$$

The difference between Equations (2.4) and (2.5) can be significant. Hence, increasing the concentration can lead to a wide range of timescales in colloidal suspensions [14].

### 2.2.1 Phase behavior of hard-sphere colloids

The phase behavior of mono-disperse colloidal suspensions as a function of  $\phi$  is shown schematically in Fig. 2.2 [14, 68]. At low volume fractions,

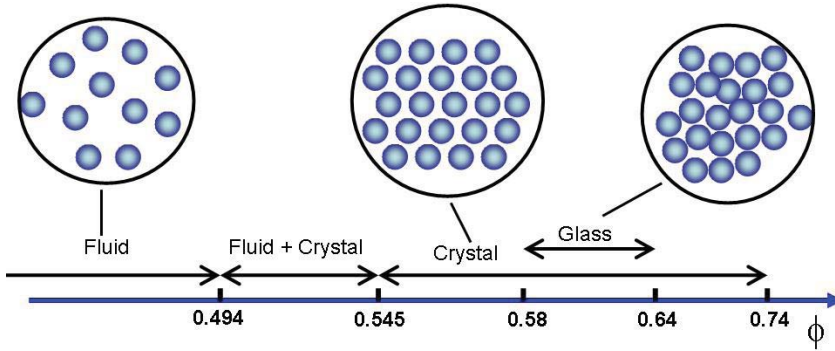


Figure 2.2: Phase diagram of uniformly sized hard spheres: various phases of hard spheres as a function of volume fraction [14, 68].

the system behaves like a dilute gas, that is, there are no structural correlations in the system. As  $\phi$  is increased, there is short-range order in the particle positions just as in a fluid. At  $\phi_f \sim 0.49$ , the freezing volume fraction, the system phase separates into coexisting fluid and crystalline phases. Above  $\phi_m \sim 0.54$ , the crystal is the thermodynamically stable phase. The crystal becomes more and more dense until it reaches a maximum close packing configuration at  $\phi \sim 0.74$ . The phases described above are equilibrium phases, where the eventual configuration of the system is determined by equilibrium thermodynamics, that is, the free energy of the system acquires a minimum. This phase behavior was confirmed experimentally by Pusey and van Meegen (Fig. 2.3) using suspensions of sterically stabilized PMMA particles (polymethyl methacrylate) [14].

However, the hard sphere systems can also exhibit non-equilibrium behavior. For example, rapid condensation of a hard-sphere fluid to  $\phi_g = 0.58$  results in a meta-stable, kinetically trapped state known as a glass, and this volume fraction is termed the glass transition volume fraction [15]. This state persists until  $\phi_{cp} \sim 0.64$ , the random close packed volume fraction, which is the maximum volume fraction that a large, random collection of spheres can attain without crystalline order.

In this thesis, we study hard-sphere colloidal glasses as a model system for amorphous materials. Dynamic light scattering experiments have shown the dynamic slow down of the suspension on intermediate time scales, and diffusive behavior on long time scales [69, 70, 71]. This dy-

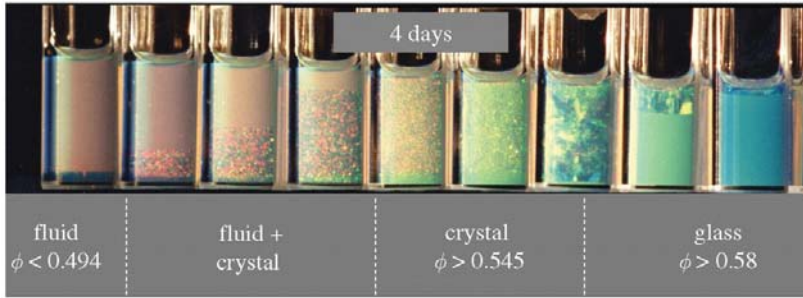


Figure 2.3: Phase diagram of colloidal hard spheres : various phases of colloidal hard spheres as function of volume fraction [14].

dynamic slow down was accurately described with the mode coupling theory, at a slightly lower volume fraction  $\phi_g = 0.52$  [72, 73, 74]. These studies have made colloidal glasses a prominent model system for the study of glasses in general.

## 2.2.2 Stabilization of hard-sphere colloids

In the present experiments we have used sterically stabilized polymethylmethacrylate particles to study hard sphere glasses. The *PMMA* is synthesized by the bulk polymerization of *MMA*(methyl methacrylate) monomers. They are transparent and colorless thermoplastic particles that are hard and stiff. The *NBD* dye is added to the particles during the synthesis, so that they are visible under laser light. The dielectric nature of *PMMA* particles in a solvent gives rise to short-range attractive van der Waals force between the spheres. So, when two particles come closer they tend to stick to each other leading to irreversible aggregation. Here, by matching the refractive index of the solvent with that of the particles, the van der Waals forces are made very small. In addition, a stabilizing mechanism is used to create a positive potential barrier between the particles to avoid flocculation. One of the ways to achieve this is steric stabilization [75, 76] of the particles where a *protective* layer of polymer/macro molecules are grafted on the surface of the *PMMA* spheres. Interactions between these layers of two adjacent particles results in a repulsion between the surfaces strong enough to suppress the van der Waals attraction. The present set of particles with a diameter of

about  $1.3\mu m$  are sterically stabilized by a layer of poly-12-hydroxystearic acid (PHSA). Thus the repulsive potential arising due to the interpenetration of polymer layers are relatively steep giving rise to 'hard-sphere' like interaction.

## 2.3 Sample Preparation

We prepare a glass using suspensions of *PMMA* particles that are  $1.3\mu m$  in diameter. They are suspended in a mixture of Cis-Decaline and Cyclo-Heptyl Bromide with a volume ratio of 1 : 3 in order to match closely the density and index of refraction of the particles with the solvent. The density matching of the particles and the solvent is needed to avoid sedimentation of the particles. The refractive index matching provides a nearly transparent sample making it suitable to visualize the individual particles in the bulk of the suspension using an optical microscope. We add the organic salt *TBAB* (tetrabutyl ammonium bromide) to the suspension to further screen the possible residual charges. The quantity of salt added is based on the  $1mM$  concentration that is to be achieved. The buoyancy-matching is very sensitive to temperature changes; the thermal expansion coefficient of the solvent exceeds that of *PMMA* by about a factor of ten and a decalin-CHB mixture of a given composition will therefore match the particle density only in a very narrow temperature range. We exploit this fact to prepare suspensions of different volume fractions by centrifuging the suspension at a speed of  $\sim 5000rpm$ , and at a temperature  $T > 35^\circ C$ , above the buoyancy matching temperature, to create a sediment that has a volume fraction close to random close packing ( $\phi_{rcp} \sim 0.64$ ). A sample of desired volume fraction is obtained by diluting the sediment at  $\phi_{rcp}$  using the density matched solvent. We typically prepare samples in the range  $\phi = 0.58 - 0.60$  to study colloidal glasses.

## 2.4 Shear cell set-up

We probe the visco-elastic properties of glasses by imposing a constant shear rate, which is of the order of the inverse relaxation time ( $\sim 10^{-5}s^{-1}$ ) of the glass. We use a home-built shear cell to apply small shear rates up to a total strain of 140% to the colloidal glass. The shear cell is designed

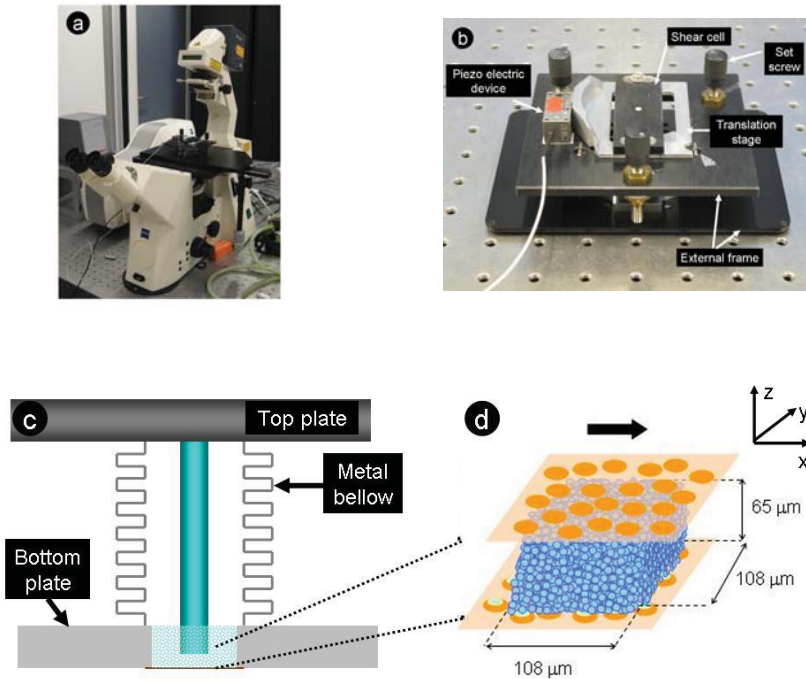


Figure 2.4: (a) An image of the shear cell mounted on the Carl Zeiss LSM-5 confocal microscope. (b) An image of the external frame that holds the piezo electric device, the translation stage and the shear cell. (c) A two dimensional section of the shear cell that shows an arrangement of a metal bellow and two parallel plates. The reservoir of colloidal particle is contained in the bottom plate. (d) An image of the roughened cover glasses that are used as boundaries, colloidal particles and the dimensions of the field of view.

to be mounted directly on the confocal microscope. Figure 2.4(a) shows a real image of the shear cell and the confocal set-up. The shear cell has an external frame that is assembled using a set of screws and springs; this arrangement provides a rigid frame for mounting the piezoelectric translation stage, and for securing the cell Fig.2.4(b). A schematic cross section of the cell in Fig.2.4(c) shows an arrangement of two parallel boundaries and a reservoir of colloidal sample. The cell essentially has two components - a *T* shaped top plate and a bottom plate that has a hole drilled through it. The top plate of the cell is fixed to the piezoelectric translation stage and the bottom plate is fixed to the frame, Fig.2.4(b).

A piece of cover glass, whose surface is made rough by sintering a layer of poly-disperse *PMMA* particles onto it, shown in Fig.2.4(d), is glued to the top and the bottom plates. This prevents boundary induced crystallization, and ensures a no-slip condition at the boundaries. The hole in the bottom plate holds a reservoir of colloidal sample of approximately  $400\mu l$ . The top boundary, which is at the free end of the cylindrical part of the top plate, is immersed in this pool of colloidal suspension. A metallic bellow, see Fig.2.4(c), is used to provide a flexible coupling between the top and the bottom plates, and to isolate the colloidal suspension from the environment, thereby preventing evaporation.

A voltage of  $0 - 150 v$  is applied to the piezoelectric device using a digital oscilloscope, to linearly displace the top plate by  $0 - 100 \mu m$ ; this differential motion of the plates imposes a uniform shear rate on the colloidal sample confined between them. By adjusting the distance  $h$  between the boundaries, using the set screws, and ramping the voltage linearly from  $0 v$  to  $150 v$ , during a time duration of  $t sec$ , we achieve a shear rate of  $\dot{\gamma} \sim 100/(h * t)$ . The coordinate axes of the system are defined with respect to the direction of shear, as shown in Fig.2.4(d); the  $x-$  axis aligns with the direction of displacement of the top boundary, the  $y-$  axis aligns with axis of shear, and the  $z-$  axis aligns with the shear gradient direction.

## 2.5 Confocal Microscopy

### 2.5.1 Optical Microscope

Optical microscopy, also referred to as “light microscopy”, uses visible light and a system of lenses to magnify images of small objects that are otherwise invisible to the naked eye. It started with the simple experiments of two Dutch spectacle makers, Zaccharias Janssen and his father Hans in the year about 1590. The modern optical microscope has evolved through the contributions of various scientists like Gallieo Galleli, Anton Leeuwenhoek and Robert Hooke in sixteenth century. Today it has become a powerful visualization tool in the domain of micron and submicron length scales for a wide variety of disciplines like Biology, nanophysics and microelectronics. Nevertheless, visualizing deep inside a sample like biological tissues or dense colloidal suspensions remain difficult by a con-

ventional optical microscope due to multiple scattering events leading to blurred images and certain artifacts. These issues were first addressed by Marvin Minsky in the 1950s who provided the basic foundation of confocal microscopy as elaborated in the section below.

## 2.5.2 Laser Scanning Microscope

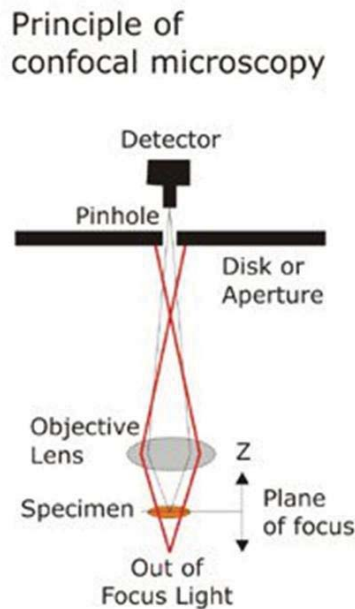


Figure 2.5: Principle of a confocal microscope. The rays that are not emanating from the focal plane are eliminated by the pinhole aperture.

In order to image in three dimensions, Marvin Minsky proposed a two-fold solution - point by point illumination of the sample to minimize aberrant rays of scattered light, as well as introduction of a pinhole aperture in the image plane eliminating all those rays emitted other than from the focal plane, thus creating a better quality image than wide field imaging where the whole object is illuminated at the same time, Fig.2.5. The light rays emerging from the pinhole are finally measured by a detector such as a photomultiplier tube. Now, constructing the image of the whole specimen in  $2D$  or  $3D$  requires scanning over a regular raster in the

specimen. While the first confocal microscopes used a translating stage, modern day confocal microscopes use lasers as light sources and scan it across the sample to visualize each point inside it- this is called Laser scanning Confocal Microscopy (*LSCM*) [77, 78]. In the present study we use a LSCM (Carl Zeiss, LSM5) with a high speed line scanning technique to obtain images of the fluorescent colloidal samples under study. The use of fluorescent particles further gives higher contrast as a filter blocks everything except the fluorescent wavelength.

### 2.5.3 Resolution

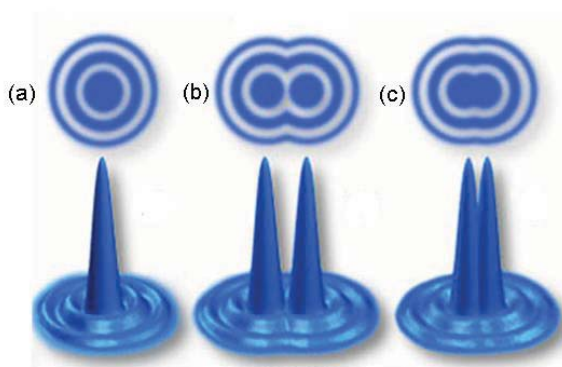


Figure 2.6: Resolution of microscope. (a) The airy disc of a single particle. (b) The overlapping airy discs of two closely spaced particles. (c) Rayleigh limit for identifying two particles as different objects.

The resolution of any optical system is the ability to clearly distinguish two separate points, or objects, as singular, distinct entities. In a confocal microscope, the image of a point-like source is a three dimensional pattern known as *point spread function* (psf) due to the diffraction through the circular aperture (pinhole). The transverse cross-section of the psf on the image plane is an Airy disc, Fig.2.6(a), whose size depends on the numerical aperture of the objective lens as well as on the wavelength of the light source. Generally, two closely spaced luminous points in the sample plane result into overlapping discs leading to an intensity distribution with two peaks as shown in Fig. 2.6(b). A minimum separation is required between the discs to create a reasonable 'dip' in

between, for the peaks to be resolved -this sets the maximum resolution of the microscope. Following Rayleigh criteria this separation is the full width half maximum (FWHM), FWHM of the airy disc (when the first minimum of an airy disc aligns with the central maximum of the second one) leading to a dip of roughly about 26%, Fig.2.6(c). For the optical setup of most commercially available confocal microscopes this separation in the lateral direction is about  $200nm$ . It is important to note that the precision of determining the position of an imaged object is different from the above discussed resolution. The position of an isolated fluorescent point-like source corresponds to the 'center of mass' of its spatially extended airy disc image. If the disc is about  $N$  pixel wide and each pixel is  $M$  micrometers across, the center of the disc can be estimated to  $Y \sim M/N$  accuracy, which is higher than the optical resolution. In the present study this uncertainty in detecting the position of a fluorescent particle is close to  $\sim 30nm$ .

## 2.5.4 Data acquisition

We image the colloidal particles in the shear cell using an objective that has a magnification of  $63x$  and a numerical aperture of 1.4. The *Zeiss LSM 5* microscope uses a line scanner to illuminate a section of the sample line by line, at a maximum of 120 frames per second (fps). The depth of the focal plane,  $Z$ , is controlled by a piezo-element mounted on the objective of the microscope. For  $3D$  imaging, a  $z$ -stack of  $2D$  images are acquired by rapidly varying the height of the objective using the piezo and simultaneously taking  $2D$  images at each  $z$ . We typically image a  $108 \times 108 \times \sim 70\mu m^3$  volume by taking 450 images at a spacing of  $0.15\mu m$  in the  $z$  direction. At a scan speed of 10fps, it takes 45 s to acquire a  $z$ -stack. We typically acquire 1 – 2 stacks every minute to follow individual particles during structural relaxation, which is of the order of  $10^5s$ . For  $2D$  imaging, we fix the position of the objective such that its focal plane is, at least,  $20\mu m$  away from the boundaries, and acquire a time series of images. Typically, the images are acquired at a rate of 10 – 20 fps to follow the short time behavior of particles in their nearest neighbor cages.

## 2.6 Particle dynamics

### Image processing

The first step in the particle tracking algorithm is the accurate identification of particle positions. The most widely used algorithm in the colloids community is that of Crocker and Grier [79], with relevant software in the public domain [80]. The algorithm identifies the particles based on the assumptions that they appear as bright spherical spots against a dark background, and the intensity maxima of the spots correspond to the center of the particle. Since we have used *PMMA* particles that are labeled with fluorescent dye, they appear as bright spots in the raw images. The undesired noise in the images is eliminated using a spatial band pass filter, which removes long wavelength contrast gradients and also short wavelength pixel to pixel noise. The particles are initially identified by locating the local intensity maxima in the filtered images. The particle coordinates are then refined to get the positions of the particle centers with a high accuracy by applying a centroiding algorithm which locates the brightness weighted center of mass (centroid) of the particles. With this refinement procedure the coordinates of the particle centers can be obtained with sub-pixel resolution down to less than 1/10 of the pixel size.

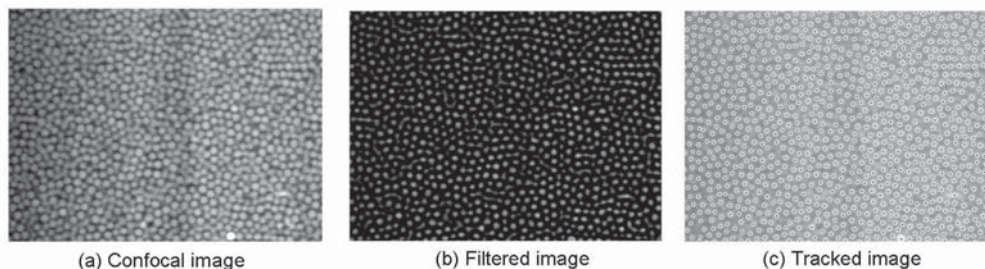


Figure 2.7: Image processing of confocal images.

An illustration of the above mentioned algorithm for locating the particle centers is shown in Fig. 2.7. A small section of the original confocal microscope images shown in Fig. 2.7(a), is filtered using a bandpass filter, Fig. 2.7(b), and particle centers are located using the intensity maximum and centroiding technique Fig. 2.7(c). A similar technique is employed to

locate the particle centers in  $3D$ . We now use these particles centers to compute the pair correlation function  $g(r)$ , which is defined as the probability of finding a particle at a distance  $r$  from a particle at the origin, in a supercooled colloidal fluid and a colloidal glass, Fig.2.8. The peak structure in the pair correlation function reveals the short-range order in the liquids and the glasses.

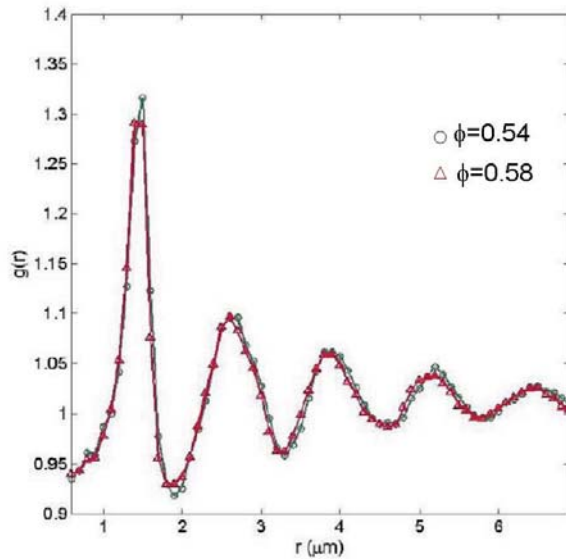


Figure 2.8: Pair correlation function of a supercooled colloidal fluid and a colloidal glass. The circular symbols indicate the supercooled fluid, while the triangles are for a glassy sample.

### Particle tracking

Using the image processing techniques described in the previous section, the particle centers are identified in all the images. The positions of the particles are then linked to construct trajectories that describe the particle motion. We use the algorithm devised by Crocker and Grier [79] for linking the particle positions. The algorithm is based on the minimization of the sum of the squared displacements of particles in two successive frames. Given the position of a particle in a frame, and all the new positions in the following frame, the algorithm reduces the complexity by considering only those particles that are in a range  $r_t$  from

the old position. When  $0 < r_t < \sigma/2$ , where  $\sigma$  is the diameter of a particle, the number of possible locations of the particle in the new frame is reduced to one. Any particle with no match in the successive frame is considered to be lost. Such particles are generally detected at the boundaries of the imaged volume where the particle moves in and out of the field of view. The algorithm repeats these steps for successive frames to link the particle positions and to construct the particle trajectories.

During a shear experiment, the images are acquired at various stages of the deformation to capture both the transient and steady state response of the system. At low shear rates,  $\dot{\gamma} \sim 10^{-5} s^{-1}$ , we typically acquire a  $z$ -stack every 1 minute for a total time duration of 25 minutes. However, at higher shear rates, we reduce the time between subsequent  $z$ -stacks to 30 seconds. Above a certain shear rate, acquiring 3D data is no longer feasible because the particles between successive stacks move more than a particle radius. This imposes a limit on the maximum shear rate to acquire 3D images.

### 2.6.1 Particle motion in a quiescent colloidal glass

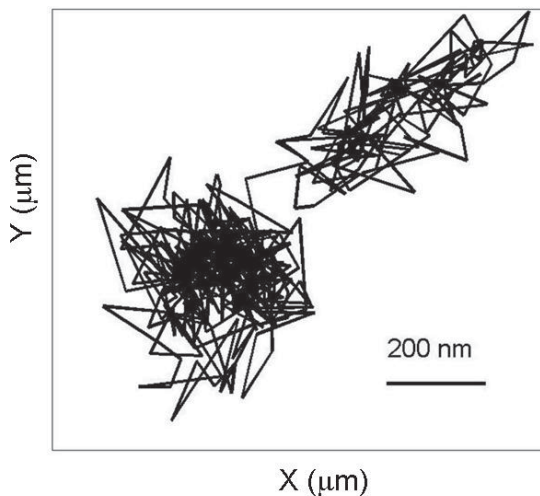


Figure 2.9: A typical trajectory of a particle in a colloidal glass ( $\phi = 0.59$ ). The image shows the cage motion and cage jump of a single particle.

A typical trajectory of a particle in a dense colloidal glass, tracked

over a time interval of  $t = 1200$  s at  $\phi = 0.59$ , is shown in Fig.2.9. The particle exhibits a caged motion on short time scales; however, over long time scales, it diffuses by moving from one cage to the other.

## 2.6.2 Analysis of particle motion in sheared colloidal glasses

In this section we outline the definition of local strain and non-affine displacement that are used in the rest of the thesis to understand the physics of sheared colloidal glasses.

### Local strain and non-Affine displacement

When a crystals (with a simple unit cell) is subject to homogeneous deformation, the particle displacements are affine, but in amorphous solids they are highly non-affine. A very simple illustration of affine and non-affine deformation is shown in Fig. 2.10. In an affine deformation, the local strain of the particles, relative to their neighbors, is the same and equal to the externally imposed strain Fig. 2.10(a), whereas in non-affine deformation, the local strain is heterogeneous, Fig. 2.10(b). The non-affine displacements are typically of the same order of magnitude as the relative affine displacements of neighboring particles, and therefore cannot be considered a small correction: ignoring them, or treating them as a perturbation, yields highly inaccurate estimates for macroscopic material properties such as the elastic moduli [38, 39, 50, 81].

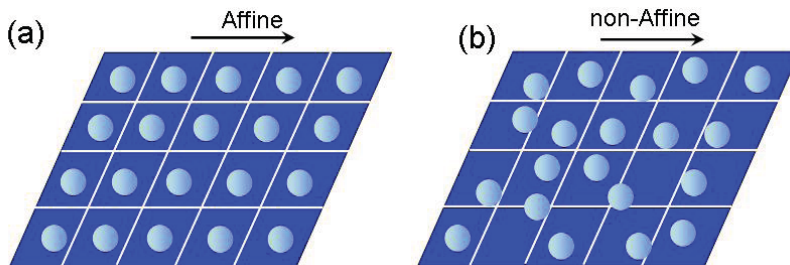


Figure 2.10: Affine (a) and non-affine (b) deformation.

In this thesis, we investigate both the affine and non-affine components of deformation in a colloidal glass. To determine the affine component, we

## 32 2. Experimental techniques

follow all particle trajectories and identify the nearest neighbors of each particle as those separated by less than  $r_0$ , the first minimum of the pair correlation function. This is illustrated in two dimensions in Fig.2.11; the thick lines and the dashed lines indicate particle positions at time  $t$  and  $t + \delta t$ , respectively, and the reference particle is colored in red, while its neighbors are colored blue. The change of nearest neighbor vectors (arrow lines) over a time interval  $\delta t$  could be related using an affine transformation  $\mathbf{\Gamma}$ . The best affine transformation  $\mathbf{\Gamma}$  is determined in such a way that it minimizes the quantity  $D^2$ , which is defined as the mean-square difference between the actual displacements of the neighboring molecules relative to the central one and the relative displacements that they would have if they were in a region of uniform deformation  $\mathbf{\Gamma}$  [37]. That is, we define

$$D^2(t, \delta t) = \sum_n \sum_i \left( r_n^i(t) - r_0^i(t) - \sum_j (\delta_{ij} + \Gamma_{ij}) \times [r_n^j(t) - r_0^j(t)] \right)^2 \quad (2.6)$$

where the indices  $i$  and  $j$  denote spatial coordinates and the index  $n$  runs over all the neighbors,  $n = 0$  being the reference particle.  $r_n^i(t)$  is the  $i$ th component of the position of the  $n$ th particle at time  $t$ . We find the  $\Gamma_{ij}$  that minimizes  $D^2$  by calculating

$$X_{ij} = \sum_n [r_n^i(t) - r_0^i(t)] \times [r_n^j(t - \delta t) - r_0^j(t - \delta t)], \quad (2.7)$$

$$Y_{ij} = \sum_n [r_n^i(t - \delta t) - r_0^i(t - \delta t)] \times [r_n^j(t - \delta t) - r_0^j(t - \delta t)], \quad (2.8)$$

$$\Gamma_{ij} = \sum_k X_{ik} Y_{kj}^{-1} - \delta_{ij}. \quad (2.9)$$

The minimum value of  $D^2(t, \delta t)$  is then the local deviation from affine deformation or the non-affine deformation during the time interval  $[t - \delta t, t]$ . This quantity is referred to as  $D_{min}^2$  in the rest of the thesis. It has been reported to be an excellent metric of plasticity that detects the local irreversible shear transformations [37]. The local strain tensor  $\epsilon_{ij}$  is obtained from the symmetric part of the deformation tensor

$$\epsilon_{ij} = \frac{1}{2}(\Gamma_{ij} + \Gamma_{ij}^T), \quad (2.10)$$

where the superscript  $T$  denotes the transpose. The strain tensor  $\epsilon_{ij}$  is of third order, and its diagonal terms give the dilation components and the non-diagonal terms give shear components of deformation.

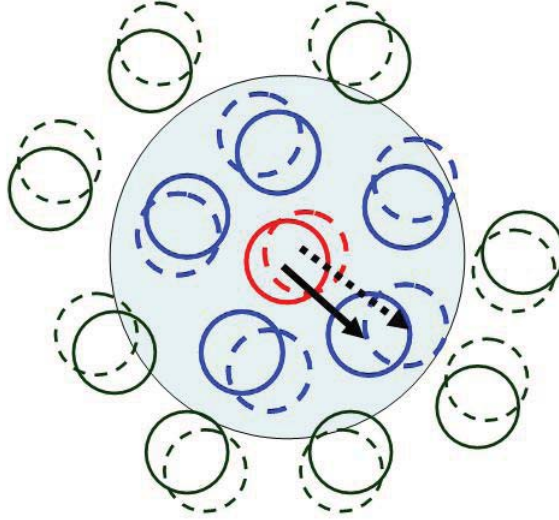


Figure 2.11: Computing the local strain. The red color indicates the reference particles and the blue color indicates its neighbors.

### Determination of non-Affine displacement using global deformation

Other definitions of non-affine deformation exist in the literature [52], and they are briefly described here. A comparison between them is made in chapter.3 of the thesis. The non-affine displacement of a particle is a measure of its diffusive motion after subtracting the convective contribution due to mean shear flow. It is defined as

$$\Delta \mathbf{r}_i^{na}(t_1, t_2) = \mathbf{r}_i(t_2) - \mathbf{r}_i(t_1) - \dot{\gamma} \int_{t_1}^{t_2} dt' y_j(t') e_x \quad (2.11)$$

where  $\dot{\gamma}$  is the shear rate and  $e_x$  is the unit vector in the  $x$  (flow) direction. The diffusive behavior follows as

$$\langle (\Delta r^{na}(0, t))^2 \rangle = 6Dt. \quad (2.12)$$

### Displacement fluctuations

A full characterization of the displacement field requires not only a distinction between the affine and non-affine components, but also a distinction between a continuous field and a fluctuating part. Motivated by the ideas in classical mechanics and kinetic theory, Goldberg and co-workers [52] have defined fluctuations of the displacement and studied their correlations. We incorporate these ideas to define a coarse grained displacement field, which is continuous, and a fluctuating part that is obtained by subtracting the continuous displacement from the actual particle displacement. The coarse grained displacement field (Eq.2.13) and fluctuation (Eq.2.14) are obtained as follows :

$$\mathbf{U}(\mathbf{r}, t_1; t_2) = \frac{1}{n} \sum_{i=1}^n \Delta \mathbf{r}_i(t_1, t_2) \Phi(\mathbf{r} - \mathbf{r}_i(t_1)), \quad (2.13)$$

$$\Delta \mathbf{r}_i^f(t_1, t_2) = \Delta \mathbf{r}_i(t_1, t_2) - \mathbf{U}(\mathbf{r}_i, t_1; t_2), \quad (2.14)$$

where  $n$  in Eq.2.13 is the number of particles in the system and  $\Phi$  is a coarse graining function. We have used a rectangular function, which can be written as a sum two Heaviside functions ( $H(x)$ ), as the coarse graining function.

$$\Phi(\mathbf{R}) = H(R + r_0) - H(R - r_0) = H(r_0^2 - R^2), \quad (2.15)$$

where  $r_0$  is the first minimum of the pair correlation function.